KSME

Springer

Journal of Mechanical Science and Technology 38 (1) 2024

Original Article
DOI 10.1007/s12206-023-1046-9

Keywords:
· Ballistic gelatin
· Non-penetrating blunt impact
· Collaborative robot
· Finite element (FE) simulation
· LS-DYNA

Correspondence to:
Yong-Sik Kim
yong@nist.gov

Citation:
Yang, T., Kim, Y.-S., Chang, J., Dagalakis, N. G. (2024). Numerical assessment of low-speed impacts on ballistic gelatin on a spring stage as a human bio-simulant. Journal of Mechanical Science and Technology 38 (1) (2024) ?~?.
http://doi.org/10.1007/s12206-023-1046-9

Received September 20th, 2022
Revised June 18th, 2023
Accepted July 16th, 2023

† Recommended by Editor Jennifer Hyunjong Shin

Numerical assessment of low-speed impacts on ballistic gelatin on a spring stage as a human bio-simulant

Taeho Yang[1], Yong-Sik Kim[2], Joonyong Chang[2] and Nicholas G. Dagalakis[2]

[1]Aerospace Performance Unit, HanYang ENG, 22, Yuseong-daero 1205 beon-gil, Yuseong-gu, Daejeon, Korea, [2]Intelligent Systems Division, Engineering Laboratory, National Institute of Standards and Technology, 100 Bureau Dr. Gaithersburg, MD, 20899, USA

Abstract Bio-simulants and finite element (FE) models have been used to investigate internal injuries caused by external impacts. As the collaboration between humans and industrial robots increases, it is important to understand the expected injuries or damage caused by collaborative robots. In this paper, FE models of the human chest were built to investigate injuries caused by low-speed non-penetrating blunt impacts from collaborative robots. The FE models were validated by comparing them with experimental results. The validated FE models were then used to calculate the maximum force and deformation that would be experienced by the human chest under different impact conditions. The results of the FE analysis were compared with relevant real human test studies.

1. Introduction

Industrial robots have been used in a variety of applications for their versatility and accuracy. Now industrial robots are very common everywhere, but many applications are still supported or assisted partially by human workers. This is because robots are good at repetitive and heavy-load tasks, but not good enough to handle unexpected errors or limited resources like small workspace, where human workers show their excellence [1]. As one method to overcome these cases, human-collaboration-robotics (HCR) [2] is utilized in various applications like factory automation [3], or medical field [4], etc.

With the improved performance, the HCR has also raised concerns about human safety [5]. As a first step for human safety in the HCR, it is important to characterize the human damages caused by robotic arms in operation or the tools held by them. It is strictly regulated and most often forbidden to run direct impact tests or drop tests on the human body, so bio-simulants and the finite element (FE) models have been widely used as replacement. The bio-simulants are hyper elastic or viscoelastic materials having similar material properties to target human tissue [6]. The simulations based on the human tissue FE models also show their usefulness in investigating the internal damage or the response of human tissue instead of forbidden human tests [7].

As human bio-simulants, a ballistic gelatin (gel or powder) is popular for its affordability and similarity to human tissue [8, 9]. The ballistic gelatin specimen is formed by mixing gelatin powder with hot water. The temperature and healing time at the post-processes can control the specimen properties to get similar mechanical behavior to human organs or muscle. Widely used processes are the Fackler formulation [10] and the NATO formulation [11]; the Fackler formulation is the mixture of the gelatin power and hot water with 1:9 ratio by volume, and then conditioned at 4 °C for two to three days [10]. The NATO formulation is the mixture of 1:4 to 1:9 ratios and cured at variable temperatures (3-20 °C) for 21 hours to 3 weeks [12]. With these formulations, ballistic gelatin or bio-simulants are also developed to investigate the behavior of the human body under various-velocity impacts including the deformation and underlying soft tissue damage [13-16]. The behavior of a ballistic gelatin specimen under high-velocity impact situations is described commonly with a hydrodynamic model [13, 14], and the quasi static and

Table 1. The maximum speed and maximum payload of commercial collaborative robots.

Manufacturer	Robot	Maximum tool center point (TCP) speed (m/s)	Maximum reach (mm)	Maximum payload (kg)	Degrees of freedom (DOF)	Weight (kg)
ABB[1]	YuMi[1]	1.5	559	0.5	14	8
Bosch[1]	APAS[1]	0.5	911	7	6	7
Denso[1]	Cobotta[1]	1.5	342.5	0.5	6+1	4
FANUC[1]	CR-4iA[1]	1	550	4	6	48
	CR-7iA[1]	1	717	7	6	53
Universal Robot[1]	UR5[1]	1	850	5	6	18.4
	UR10[1]	1	1300	10	6	28.9
Rethink robotics[1]	Baxter[1]	0.6-1	1210	2.2	14	74.8

[1]Certain trade names and company products are mentioned in the text or identified in an illustration to adequately specify the experimental procedure and equipment used. In no case does such an identification imply recommendation or endorsement by the National Institute of Standards and Technology, nor does it imply that the products are necessarily the best available for the purpose.

low-velocity impact situations with the hyper-elastic models [15, 16].

The details and the special features for the HCR are well summarized from biomechanical limits for power and force limited (PFL) collaborative robot applicationsin ISO Technical Specification - TS15066 Robots and robotic devices – collaborative robots [17]. With the HCR standards,the relevant characteristics for the HCR application are summarized in Table 1, which are extracted from the popular commercial robots. The details in Table 1 can be found on the website from each manufacturer. In Table 1, the maximum speed ranges from 0.5 m/s to 1.5 m/s with the average of 1.02 to 1.06 m/s, and the average maximum payload is 4.5 kg. All collaborative robots provide at least 6 DOF motion and the average reachable range of 804.9 mm.

Considering the maximum speed and the average force values in Table 1, the HCR environment can be categorized as low-speed non-penetrating high inertia impact. In addition, Table 1 can be used as a reference for the impact test simulating the HCR environments.

In this paper, the FE models are proposed to simulate the material properties for human body, especially the chest, under low-speed non-penetrating high inertia impact condition for the HCR environment [18, 19]. The constructed FE models are numerically evaluated with other studies in Sec. 2 and utilized to investigate the damage to human chest and compared with other studies in Sec. 3.

2. Mathematical models for the ballistic gelatin specimen

The FE models proposed in this paper is a stack-up structure; a hyper-elastic specimen, a ballistic gelatin is placed on top of a spring stage. Human chest is stiffer than a ballistic gelatin, because human chest has bone structure as well as muscle and skin. Due to this limit, the spring stage is utilized to result in the stiffness and the deformation similar to human chest by adjusting its stiffness and motion range. Based on this approach, the FE modeling of a ballistic gelatin is explained in Sec. 2 and the whole model is described and numerically evaluated in Sec. 3.

2.1 The Ogden and the Mooney-Rivlin model as bio-simulant model

Two hyper-elastic models are utilized to describe the mechanical behavior of the ballistic gelatin specimen. The Mooney-Rivlin model (W_{MR}) and the Ogden model (W_{OG}) strain energy density functions are selected for their popularity and accuracy. The Mooney-Rivlin model is based on strain invariants and the Ogden model is based on principal stretches [20]. In these cases, the first-order equation of W_{MR} and W_{OG} can be expressed as:

$$W_{MR} = C_{10}(I_1 - 3) + C_{01}(I_2 - 3) \tag{1}$$

$$W_{OG} = \frac{\mu_1}{\alpha_1}\left(\lambda_1^{\alpha_1} + \lambda_2^{\alpha_1} + \lambda_3^{\alpha_1} - 3\right) \tag{2}$$

where, C_{10} and C_{01} are constants, and I_1 and I_2 are invariants of W_{MR}. μ_1 and α_1 are constants, and λ_1, λ_2, λ_3 are principal stretch of W_{OG}. I_1 and I_2 in Eq. (1) are defined as:

$$I_1 = \lambda_1^2 + \lambda_2^2 + \lambda_3^2,\ I_2 = \lambda_1^2\lambda_2^2 + \lambda_2^2\lambda_3^2 + \lambda_3^2\lambda_1^2 . \tag{3}$$

The strain energy function in terms of the strain invariants in Eq. (1) or in terms of the principal stretches in Eq. (2) should be derived from the stress-stretch function. In this case, the Cauchy stress tensor (σ_i) can be calculated by using Eqs. (4) and (5) expressed below:

$$\sigma_i = \bar{P} + 2\frac{\partial W_{MR}}{\partial I_1}\lambda_i^2 - 2\frac{\partial W_{MR}}{\partial I_2}\lambda_i^{-2} \tag{4}$$

$$\sigma_i = \bar{P} + \frac{\partial W_{OG}}{\partial \lambda_i}\lambda_i \tag{5}$$

where, $\bar{P}$ is an indeterminate multiplier and can be eliminated because it is assumed that ballistic gelatin is incompressible

Table 2. The drop heights (h), the impact velocities (V_{impact}) and the parameters of the corresponding mathematical models for 10 % ballistic gelatin.

Drop height (h_{drop})	Impact velocity (V_{impact})	The Mooney-Rivlin model		The Ogden model	
		C_{10}	C_{01}	μ_1	α_1
20.5 mm	0.59 m/s	2.78×10^4	2.83×10^4	2.98×10^4	3.82
30.5 mm	0.70 m/s	3.20×10^4	3.30×10^4	3.87×10^4	3.65
40.5 mm	0.82 m/s	4.41×10^4	4.61×10^4	5.59×10^4	3.58
50.5 mm	0.89 m/s	4.29×10^4	4.64×10^4	7.48×10^4	3.14

material [20]. Then the Cauchy stress tensor of W_{MR} and W_{OG} in Eqs. (4) and (5) can be substituted to Eq. (6).

$$P_i = \sigma_i \lambda_i^{-1}, i \in 1, 2, 3 . \tag{6}$$

The stress-stretch function of W_{MR} and W_{OG} can be obtained from the uniaxial compression test of ballistic gelatin. Each term of the stress-stretch function is based on the Ref. [21] and its stretch terms can be expressed as Eq. (7) and the stress terms can be as Eq. (8).

$$\lambda_1 = \lambda, \lambda_2 = \lambda_3 = \lambda^{-1/2} \tag{7}$$
$$\sigma_1 = \sigma_S, \sigma_2 = \sigma_3 = 0 . \tag{8}$$

From Eqs. (7) and (8), the several parameters are summarized to the two parameters: λ and σ. To find the parameters, the strain-stress curve is experimentally measured from the uniaxial compression test in the following section.

2.2 Uniaxial compression test to build the mathematical models

The schematic diagram of the uniaxial compression test set-up used in this paper is shown in Fig. 1. The testing machine is a drop tower impact machine [6], where the impact plate moves along the vertical rail and is designed to accelerate by gravity. The impact velocity is controlled by the drop height (h) indicated by the caption in Fig. 1. The specimen is a ballistic gelatin gel of cylindrical shape with a diameter of 25.4 mm and a height of 12.5 mm following the American Society for Testing and Materials (ASTM) standard test methods for rubber property [22]. The impact plate is a square plate larger than the specimen. Three sensors are also attached to the impactor to monitor the response from a specimen: the linear variable differential transformer (LVDT) sensor for displacement, accelerometers for acceleration, and the loadcell for force.

With this experimental set-up, the impact plate hits the specimen and the force, and the displacement of the impact plate was monitored in real-time. The specimen in the test is shown in Fig. 1(b) where the upper image is before the impact and the lower image is after the impact. This test was repeated multiple times to obtain the strain-stress relationship for four different impact velocities listed in Table 2. Based on this relationship, the two mathematical models describing the behavior of the ballistic gelatin are built by curve fitting methods based on both the W_{MR} in Eq. (7) and the W_{OG} in Eq. (8) and iterative search-

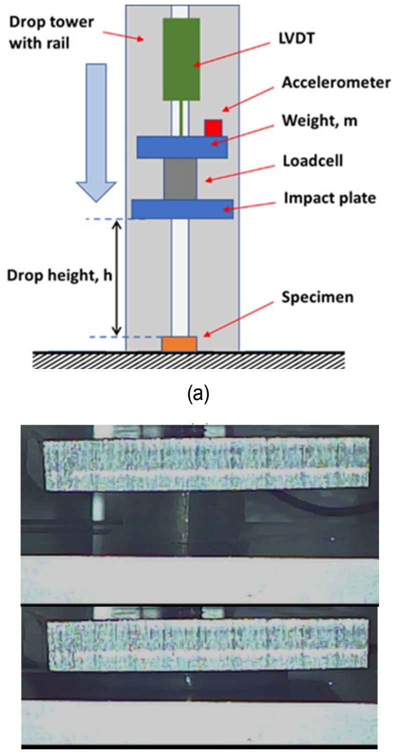

(a)

(b)

Fig. 1. The uniaxial compression test: (a) test set-up diagram; (b) the intact shape before impact and the maximum compressed shape after impact.

ing is used to find appropriate parameters for both models. The parameters corresponding to the mathematical models are listed in Table 2 with the drop heights(h) and the impact velocities (V_{impact}) for 10 % ballistic gelatin. Both constants (C_{10}, C_{01}) of the Mooney-Rivlin model increase when the impact velocity increases. On the other hand, μ_1 of the Ogden model increases like the constants of the Mooney-Rivlin model, but α_1 of the Ogden model decreases when the impact velocity increases. This shows that the parameters in the Mooney-Rivlin and the Ogden model are considerably affected by the impact velocity.

2.3 The evaluation of the mathematical models

The constructed FE models are numerically evaluated by comparing them with the relevant uniaxial compression experiments under the same experimental condition. The simulation models are designed based on the parameters in Table 2 and illustrated in Fig. 2. This uniaxial compression test model

Table 3. The maximum acceleration comparison between the experiments and the FE simulations.

Drop height (mm)	Impact velocity (m/s)	The measured maximum acceleration (m/s^2)	The Mooney-Rivlin model		The Ogden model	
			The calculated maximum acceleration (m/s^2)	Error (%)	The calculated maximum acceleration (m/s^2)	Error (%)
20.5	0.59	104.97	112.98	7.63	115.25	9.79
30.5	0.70	139.12	135.95	-2.28	149.46	7.43
40.5	0.82	161.49	179.30	11.03	183.90	13.88
50.5	0.89	180.60	205.72	13.91	207.32	14.80

Table 4. The maximum force comparison between the experiments and the FE simulations.

Drop height (mm)	Impact velocity (m/s)	The measured maximum force (N)	The Mooney-Rivlin model		The Ogden model	
			The calculated maximum force (N)	Error (%)	The calculated maximum force (N)	Error (%)
20.5	0.59	343.10	368.18	7.31	379.12	10.50
30.5	0.70	453.88	414.81	-8.61	473.07	4.23
40.5	0.82	530.57	544.60	2.65	577.19	8.79
50.5	0.89	601.15	623.99	3.80	643.98	7.13

consists of an impact plate, a ground plate, and a ballistic gelatin specimen. All FE simulations were processed on a commercial FE simulation software, LS-DYNA[1] [23] with explicit dynamic condition and the mesh size of 1 mm is applied to all elements. The impact plate is made up with a shell element and is designed to move up and down to apply an impact on top of the test specimen. The ground plate is also made up with a shell element and a fixed boundary condition is applied. The ballistic gelatin specimen is built with a solid element andthe impact velocity (V_{impact}) is applied to the impact plate, which is set as the excitation of the simulation. The V_{impact} is four impact velocities listed in Table 2.

After a series of simulations, the FE simulation results were compared with the experimental data for four different impact velocities. Among various results, Fig. 3 shows the two acceleration results for the two impact velocities, where the experimental data are in blue solid line, the FE simulation results based on the Mooney-Rivlin model (FE_{MR}) in grey dotted line, and the FE simulation results based on the Ogden model (FE_{OG}) in orange dotted line. Both FE_{MR} and FE_{OG} show very similar trends with the experimental data from the initial contact to the maximum deformation. The time from the initial contact to the maximum deformation ranges from 15 ms to 25 ms. However, the experiment shows vibrations which are not well predicted by the FE simulations after the maximum deformation. From this comparison, it appears that the FE simulation results are valid enough to evaluate the expected maximum deformation, acceleration, and force, because the first impact causes the maximum deformation and the maximum force.

For the numerical comparison, the maximum acceleration values are extracted from the FE simulation and the experiments and then summarized in Table 3 for the maximum acceleration differences from four different impact velocities. In Table 3, the FE_{MR} has the average error of 8.71 % and the FE_{OG} has the average error of 11.5 % from the experiments.

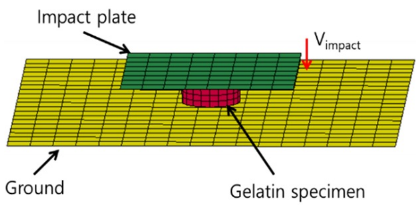

Fig. 2. The FE model of the uniaxial compression test.

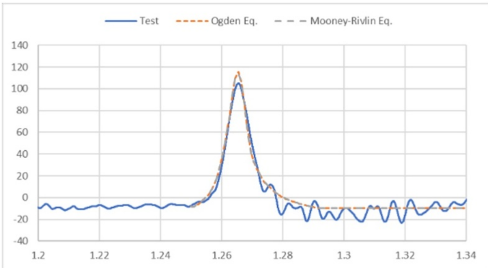

(a)

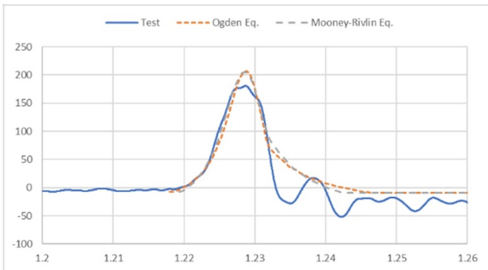

(b)

Fig. 3. Time history on the acceleration of the impact plate for four different impact velocities: (a) V_{impact} = 0.59 m/s; (b) V_{impact} = 0.89 m/s.

In a similar way, the maximum force values are also compared with the experimental results and listed in Table 4 and the maximum displacement difference in Table 5. The average

Table 5. The maximum compression deformation comparison between the experiments and the FE simulations.

Drop height (mm)	Impact velocity (m/s)	The measured maximum compression (mm)	The Mooney-Rivlin model		The Ogden model	
			The calculated maximum compression (mm)	Error (%)	The calculated maximum compression (mm)	Error (%)
20.5	0.59	8.42	8.06	-4.23	8.07	-4.18
30.5	0.70	8.71	6.59	-24.43	8.19	-6.02
40.5	0.82	8.76	6.45	-26.35	8.04	-8.21
50.5	0.89	9.24	6.71	-27.35	8.06	-12.77

force error of the FE_{MR} is 5.6 % and that of the FE_{OG} is 7.7 %, the average compression deformation error of the FE_{MR} is -20.6 % and that of the FE_{OG} is -7.8 %. From Tables 3-5, it appears that both the FE_{OG} model and the FE_{MR} model show similar error less than 10 % level in acceleration and force, but there is a noticeable difference in compression deformation, where the FE_{OR} model shows similar level of error compared to acceleration or force, but the FE_{MR} is far less accurate.

3. Human chest model simulation

3.1 Human bio-simulant model

After the numerical evaluation, the two FE models were applied to the whole model to find their usability in a HRC environment. For this purpose, a human chest affected by typical collaborative robotis simulated by both FE models, because it is expected to be common to expose human chest or back to robots in the HCR environment. Among various approaches to builda relevant human chest bio-simulant model, the stack-up model [24] is adapted and used for its simplicity and affordability in this paper. For the stack-up model, a ballistic gelatin sample is placed on top of one degree of freedom (DOF) spring stage. An artificial leather is placed on top of a ballistic gelatinas a skin simulation.

The corresponding diagram of the model used is illustrated in Fig. 4(a), where the combination of the ballistic gelatin specimen indicated by the subscript 2 and the spring stage indicated by the subscript 1. The stiffness of the spring stage is controlled by the number of springs and their stiffness shown in Fig. 6(b). The thickness of the ballistic gelatin specimen and the stiffness of the spring stage are controlled to build the load-deformation curve close to human chest stress-strain relationship [25].

Fig. 4(b) is the stress-strain curve from the layered puck model built in this paper, which is obtained a commercial universal compression testing machine [26]. In this case, there are three different stiffness zones indicated by the arrows: 14.54 N/mm for the AB zone, 27.00 N/mm for the BC zone, and 36.79 N/mm for the CD zone. From the stiffness or the slope, the ballistic gelatin specimen is dominant at the AB zone and the spring stage play an important role at the CD zone. The BC zone is mixed between them. From several trials-and-errors, the ballistic gelatin thickness is decided to be 30 mm, which was made by the Fackler formulation, and the artificial

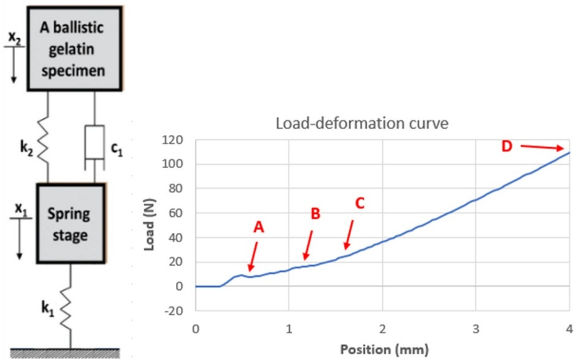

(a) (b)

Fig. 4. The bio-simulant: (a) the schematic model; (b) the load-deformation curve.

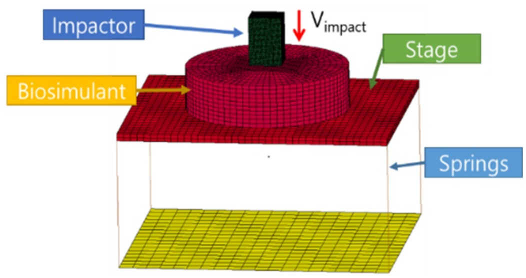

Fig. 5. The FE model of human chest bio-simulant model.

leather is placed on top of the ballistic gelatin specimen as human skin surrogate. In addition, eight to eleven springs are installed in the spring stage to control the total stiffness of the stage from 25 to 45 N/mm. With this set-up, the strain-stress curve of this bio-simulant model gets closer to that of human chest or back shoulder in Refs. [25, 27].

3.2 The FE simulations for human bio-simulant

Fig. 5 is the capture of the FE simulation model for the human chest bio-simulant model in Fig. 4(a). In the FE simulation, the material properties of the ballistic gelatin specimen are described by both FE_{MR} and FE_{OG} models. The skin is represented by the shell element with the thickness of 1.5 mm and its material properties are listed in Table 3 in Ref. [28]. The friction coefficients between the bio simulant and the impactor and between the bio simulant and the stage are cited from Ref.

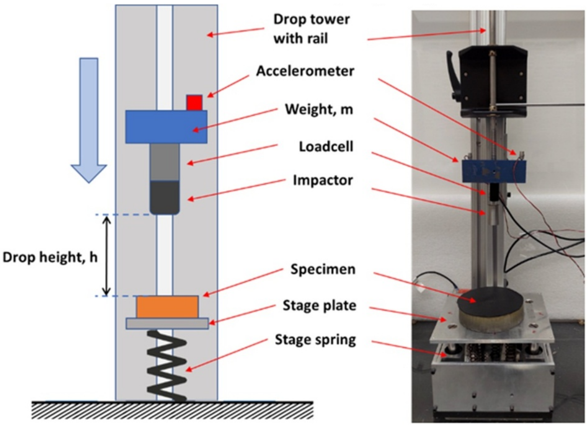

(a)

(b)

Fig. 6. The impact test of the bio-simulant: (a) the schematic diagram and the experimental set-up; (b) the springs installed underneath the stage.

[29]. The spring in the stage is modeled as a discrete element in the FE simulation. The motion of the spring stage is constrained and allowed only to move along the impact direction.

The excitation for this FE simulation is modeled with an external blunt impactor; the impactor is a rectangular column with the cross section of 19 mm×24 mm, and the length of 35 mm. The dead weight is set to be 3.3 kg and the impact weight is controlled to generate an impact force between 120 N and 180 N, which are in the range of the maximum permissible forces in ISO/TS 15066 [27] and under the average force values in Table 1. The schematic diagram and the impact testing apparatus is shown in Fig. 6(a) showing that the layered puck bio-simulant artifact placed under a drop tower type impact machine [6]. Fig. 6(b) show the spring stage with the installed springs, which are used to control the stiffness of the spring stage.

The multiple impact tests were performed with the equipment shown in Fig. 6(a), and the acceleration, force, and the deformation were measured in real-time for variousimpact velocities. Fig. 7 is the comparison between the FE simulations and the experimental impact test results, where the impact test data are plotted in solid blue lines, the FE_{MR}in dotted grey lines, and the FE_{OG}in dotted orange lines. The acceleration is in Fig. 7(a), the force in Fig. 7(b), and the displacement of the impactor in Fig. 7(c). The FE simulations in this paper tend to predict larger

Table 6. Material properties of the skin in the simulation [28].

Young's modulus (MPa)	0.85
Poisson's ratio	0.46
Density (kg/m^3)	1100

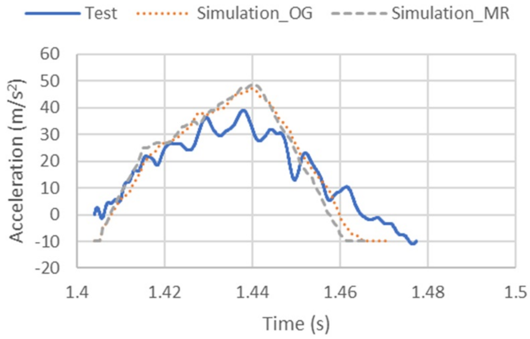

(a)

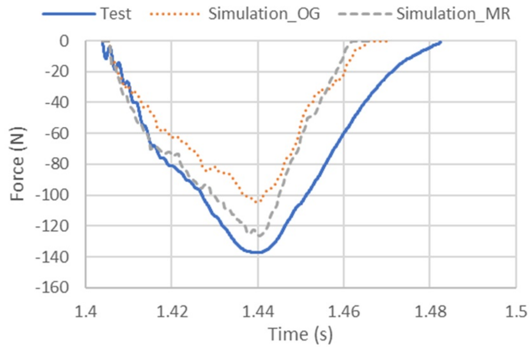

(b)

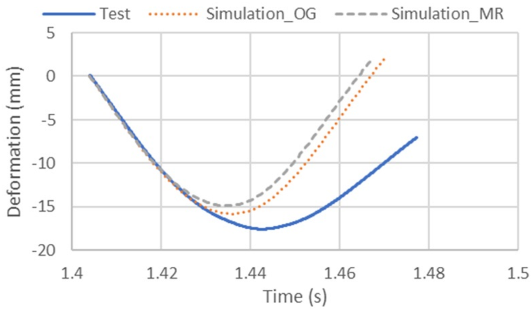

(c)

Fig. 7. Comparison on results between the impact test and the FE simulation with the FE_{MR} and the FE_{OR} models: (a) acceleration; (b) force; (c) displacement.

maximum or peak values of the acceleration and the impact force, than the experiments. This is partly because the FE simulations are based on ideal cases without any friction among the movable components. The comparison also shows that the FE_{OG} tends to show slightly larger values in displacement than the FE_{MR}, partly because the Ogden model is designed for large deformations of 200 % to 300 % of strain rate. Depending on the impact situation, both models can be utilized depending on the deformation range. From this observation,

Table 7. Comparison of the maximum impact force and the maximum compressive deformation between the test data and the FE_{OG}.

Impactor	Maximum deformation (mm) and force (N)	Average difference	Maximum difference	Minimum difference
Circular shape 20 mm diameter	Maximum deformation (mm)	-0.586 (-2.49 %)	0.268 (1.11 %)	-2.033 (-8.41 %)
	Maximum force (N)	-1.657 (-1.68 %)	1.908 (1.90 %)	-4.082 (-4.06 %)
Circular shape 13 mm diameter	Maximum deformation (mm)	0.021 (0.08 %)	1.376 (5.52 %)	-1.535 (-6.16 %)
	Maximum force (N)	-2.424 (-2.29 %)	8.546 (8.09 %)	-13.613 (-12.88 %)
Circular shape 10 mm diameter	Maximum deformation (mm)	2.809 (10.16 %)	4.055 (14.68 %)	0.429 (1.55 %)
	Maximum force (N)	-1.144 (-1.05 %)	3.528 (3.25 %)	-5.236 (-4.82 %)
Rectangular shape 19 mm×24 mm	Maximum deformation (mm)	0.685 (3.03 %)	1.358 (6.01 %)	0.138 (0.76 %)
	Maximum force (N)	5.341 (4.98 %)	8.501 (7.92 %)	-0.048 (-0.04 %)
Rectangular shape 9.5 mm×12 mm	Maximum deformation (mm)	0.463 (1.56 %)	4.817 (16.17 %)	-2.547 (-8.55 %)
	Maximum force (N)	0.988 (0.94 %)	7.133 (6.78 %)	-5.321 (-5.06 %)

Table 8. Comparison on the maximum force between the FE simulation and external study.

Impactor	Deformation (mm)	Maximum force (N)	V_{impact} (m/s)	Weight (kg)
Cylindrical shape of 20 mm diameter	21-26 mm	98-103	0.89	3.3
Cylindrical shape of 13 mm diameter	24-27 mm	102-106	0.89	3.3
Cylindrical shape of 10 mm diameter	25-30 mm	105-110	0.89	3.3
Rectangular shape of 19 mm×24 mm	20-25 mm	99-107	0.89	3.3
Rectangular shape of 9.5 mm×12 mm	27-31 mm	100-105	0.89	3.3
Disk shape at LWRIII [19]	10-13 mm	90-100	0.7	4
Disk shape at LWRIII [19]	15-20 mm	150-160	1	4
Disk shape at LWRIII [19]	15-25 mm	200-210	1.5	4
Square shape of 14 mm×14 mm [25]	12-57 mm	3.4-155	1.25	5.8

Fig. 7 shows that the FE simulation show similar trend line with the experiment.

Among various FE simulation results, the maximum force or maximum deformation are critical to human safety. Thus, the maximum values extracted from the FE_{OG} simulationsare compared with the experiments and listed in Table 7. In Table 7, the maximum values were measured for various impact tools including the circular impact plates of 20 mm, 13 mm, and 10 mm diameter, and the rectangular impact plates of 19 mm×24 mm, 9.5 mm×12 mm at the impact velocity of 0.82 m/s. After the tests more than ten times,the average forces difference ranges from -5.2 N to 4.89 N and their standard deviation is from 0.43 N to 7.01 N. Considering that the maximum force ranges from 100 N to 120 N, their average error is less than 5 % difference. This comparison shows that the FE model proposed here can be used to predict the response of the bio-simulant model.

3.3 The comparison with external research

The impact tests and the FE simulation results discussed in this paper are also compared with independent studies. Since it is rare to find real human test under the same test conditions due to various social and ethical restrictions, the similar studies on human chest or body are included with the explanation about the difference. The details are summarized in Table 8 with the impact condition and the measured deformation and force. In Table 8, the first five rows come from the proposed FE models in this paper for comparison and the others from different sources. Among them, the test by Sami et al. [19] is human chest impact test with a robotic arm and shows similar test condition used in this paper, based on its impact velocity ranging from 0.2 m/s to 2 m/s. The details are listed in Table 8 showing that the FE models in this paper show similar values measured from other studies, although the detail test environments are not the exact same. This comparison indicates that the proposed FE models have the capabilities to show the reasonable results.

4. Conclusions

In this paper, the FE models areproposedfor human body, especially human chest under low-speed non-penetrating high inertia impact condition to simulate the expected damages or human injuries in the HCR environment. For the reasonable simulation, the FE models consists of a hyper-elastic component and a spring stage. The hyper-elastic material used in this paper is ballistic gelatin gel for human body and is placed on a spring stage.

The FE models for a ballistic gelatin are constructed based on two hyper-elastic models; the Mooney-Rivlin FE model and the Ogden FE model to simulate the large deformation of human muscle with the difference error less than 15 %. The comparison with the experimental results shows that the Mooney-Rivlin model is good at the deformation up to 100 % and the Ogden model is better at deformation larger than 200 %.

Since it is not easy to meet the mechanical behavior of human body by a ballistic gelatin only, the spring stage is also utilized to simulate the mechanical response of human chest, especially the stiffness and the deformation. The spring stage has multiple number of springs inside, so the number of springs, the spring length, and the stiffness of each spring are utilized to find the appropriate ratio.

After the design process, the constructed FE models are then evaluated in two ways; the ballistic gelatin model only is numerically evaluated by the impact tests in Fig. 6 showing that the force and the deformation error range is less than 20 % depending on the impact velocities. After this evaluation, the whole model is compared with the external studies, showing that both are in similar force and deformation level.

From this observation and the comparisons, the proposed FE models can be one approach to investigate the internal stress distribution or the mechanical behavior at the impact moment carefully. Since real human impact tests are very rare, the proposed model will be evaluated whenever new human tests are reported. Especially, the proposed FE models can be utilized to human head or abdomen which are also vulnerable to external impacts in HCR environment.

Nomenclature

FE : Finite element
HRC : Human-robot collaborative
DOF : Degree of freedom
OG : Ogden
MR : Mooney-Rivlin
V_{impact} : Impact velocity
H_{drop} : Drop height
LVDT : Linear variable differential transformer
TCP : Tool center point
PFL : Power and force limit
ASTM : American Society for Testing and Materials

References

[1] A. Kanazawa, J. Kinugawa and K. Kosuge, Adaptive motion planning for a collaborative robot based on prediction uncertainty to enhance human safety and work efficiency, *IEEE Transactions on Robotics*, 35 (4) (2019) 817-830.
[2] E. Guizzo and E. Ackerman, How rethink robotics built its new baxter robot worker, *IEEE Spectrum*, 2012 (2012) 18.
[3] M. Bélanger-Barrette, *Collaborative Robot*, ROBOTIQ (2015).
[4] M. Valori, A. Scibilia, I. Fassi, J. Saenz, R. Behrens, S. Herbster, C. Bidard, E. Lucet, A. Magisson, L. Schaake, J. Bessler, G. B. Prange-Lasonder, M. Kühnrich, A. B. Lassen and K. Nielsen, Validating safety in human-robot collaboration: standards and new perspectives, *Robotics*, 10 (2021) 65, https://doi.org/10.3390/robotics10020065.
[5] S. Robla-Gómez, V. M. Becerra, J. R. Llata, E. González-Sarabia, C. Torre-Ferrero and J. Pérez-Oria, Working together: a review on safe human-robot collaboration in industrial environments, *IEEE Access*, 5 (2017) 26754-26773, doi: 10.1109/ACCESS.2017.2773127.
[6] N. G. Dagalakis, J. M. Yoo and T. Oeste, Human-robot collaboration dynamic impact testing and calibration instrument for disposable robot safety artifacts, *Industry Robotics*, 43 (3) (2016) 328-337.
[7] J. Zhang, N. Yoganandan, F. A. Pintar and T. A. Gennarelli, Finite element analysis of penetrating head injury, *Proceedings of the ASME 2003 International Mechanical Engineering Congress and Exposition*, *Advances in Bioengineering*, Washington, DC, USA, 15-21 (2003) 193-194, https://doi.org/10.1115/IMECE2003-42978.
[8] B. P. Kneubuehl, *Wound Ballistics: Basics and Applications*, 4th ed., Springer-Verlag (2011).
[9] D. S. Cronin and C. Falzon, Characterization of 10 % ballistic gelatin to evaluate temperature, aging and strain rate effects, *Exp. Mech.*, 51 (2010) 1197e206.
[10] M. L. Fackler and J. A. Malinowski, Ordnance gelatin for ballistic studies, *The American Journal of Foresnic Medicine and Pathology*, 9 (1988) 218-219.
[11] J. Jussila, Wound ballistic simulation: assessment of the legitimacy of law enforcement firearms ammunition by means of wound ballistic simulation, *Thesis*, Second Department of Surgery, University of Helsinki, Finland (2005).
[12] N. R. Maiden, W. Fisk, C. Wachsberger and R. W. Byard, Ballistics ordnance gelatine - how different concentrations, temperatures and curing times affect calibration results, *J. Forensic Leg Med.*, 34 (2015) 145-150, doi: 10.1016/j.jflm.2015.05.019.
[13] A. Airoldi and B. Cacchione, Modelling of impact forces and pressures in lagrangian bird strike analyse, *Int. J. Impact. Eng.*, 32 (2006) 1651-1677.
[14] G. J. Appleby Thomas, P. J. Hazell, J. M. Wilgeroth, C. J. Shepherd, D. C. Wood and A. Roberts, On the dynamic behavior of three readily available soft tissue simulants, *J. Appl. Phys.*, 109 (084701) (2011) 1-6.
[15] D. S. Cronin and C. Falzon, Dynamic characterization and simulation of ballistic gelatin, *Proceedings of the SEM Annual Conference*, Society for Experimental Mechanics, New Mexico, USA (2009).
[16] L. Liu, Z. Jia, X. L. Ma and Y. R. Fan, Analytical and experimental studies on the strain rate effects in penetration of 10 wt % ballistic gelatin, *J. Phys. Conf. Ser.*, 451 (2013) 012035.
[17] ISO/TS 15066:2016, *Robots and Robotic Devices - Collaborative Robots*, ISO, 2 (2016) 1-5.
[18] C. Van Sligtenhorst, D. S. Cronin and G. Wayne Brodland, High strain rate compressive properties of bovine muscle tissue determined using a split Hopkinson bar apparatus, *J. Biomech.*, 39 (10) (2006) 1852-1858, doi: 10.1016/j.jbiomech.

2005.05.015.
[19] S. Haddadin, A. Albu-Schäffer and G. Hirzinger, The role of the robot mass and velocity in physical human-robot interaction - part I: non-constrained blunt impacts, *2008 IEEE International Conference on Robotics and Automation Pasadena*, CA, USA (2008) 19-23.
[20] B. Giovanni, V. Rocco, P. Marcello and V. Gabriele, Chapter 6: Hyperelastic modeling of rubber-like photopolymers for additive manufacturing processes, *Rapid Prototyping Technology-Principles and Functional Requirements*, IntechOpen (2011).
[21] R. W. Ogden, Large deformation isotropic elasticity: on the correlation of theory and experiment for incompressible rubber-like solids, *Proceedings of the Royal Society of London A-326* (1972) 565-584.
[22] ASTM D395-16, *Standard Test Methods for Rubber Property Compression Set*, ASTM International (2017).
[23] F. Chen, R. Chen and B. Jiang, The adaptive finite element material point method for simulation of projectiles penetrating into ballistic gelatin at high velocities, *Engineering Analysis with Boundary Elements*, 117 (2020) 143-156, https://doi.org/10.1016/j.enganabound.2020.03.022.
[24] GTE, *Kraft-Druck-Messsysteme für kollaborierende Roboter*, GTE, https://www.gte.de/produktuebersicht/kraftmesssysteme-fuer-kollaborierende-roboter/.
[25] R. Behrens, G. Pliske, M. Umbreit, S. Piatek, F. Walcher and N. Elkmann, A statistical model to determine biomechanical limits for physically safe interactions with collaborative robots, *Front. Robot. AI*, 8 (2022) DOI: 10.3389/frobt.2021.667818.
[26] J. Markarian, Mechanical testing suppliers strive for accuracy and reproducibility, *Plastics, Additives and Compounding*, 11 (3) (2009) 18-22.
[27] ISO/TS 15066:2016, *Robots and Robotic Devices - Collabo-Rative Robots*, ISO (2016).
[28] Z. Cheng, J. A. Smith, J. A. Pellettiere and S. M. Fleming, Considerations and experiences in developing a finite element buttock model for seating comfort analysis, *SAE Technical Paper* (2007) 2017-01-2458.
[29] F. A. Urrea, F. Casanova, G. A. Orozco and J. J. García, Evaluation of the friction coefficient, the radial stress, and the damage work during needle insertions into agarose gels, *J. Mech. Behav. Biomed. Mater.*, 56 (2016) 98-105, doi: 10.1016/j.jmbbm.2015.11.024.

Taeho Yang is a Manager at EPC BU/ Aerospace PU, HANYANG ENG CO., LTD. He received his Ph.D. degree in Mechanical Design and Mechatronics Engineering in 2015. From 2017 to 2019, he worked at National Institute of Standards and Technology as Guest Researcher. Dr. Yang's research interests include impact analysis on structures with the hyper-elastic material and optimum design of structures in the aerospace industry.

Joonyong Chang serves as a Guest Researcher at the National Institute of Standards and Technology (NIST) in the United States. He earned his Master of Science degree in Mechanical Design Engineering from Chungnam National University, South Korea, in 2016. Between 2015 and 2018, Mr. Chang held a position at the Korea Atomic Energy Research Institute (KAERI), and from 2018 to 2019, he worked as a researcher at the Korea Advanced Institute of Science and Technology (KAIST). Mr. Chang's research is primarily focused on assessing and analyzing the static and dynamic behavior of structures and materials under various conditions.

Nicholas G. Dagalakis received his M.S., Eng.D. and Ph.D. degrees from the Massachusetts Institute of Technology (MIT), Cambridge Massachusetts, U.S.A. and his Diploma from the National Technical University of Greece, Athens, in Mechanical and Electrical engineering. He has worked for two small companies, MIT as a Research Associate and the University of Maryland in College Park, as an Assistant Professor. He is a full-time research staff at the National Institute of Standards and Technology (NIST) in Gaithersburg Maryland. He has conducted research in Electrical Generation, Biomedical Engineering, Industrial Robotics design and control, performance measurement, and safety, High Precision Micro/Nano Manufacturing, Sensors, and Standards. He has 43 journal and 62 conference publications, 3 book chapters and 5 patents. He is an IEEE senior member and has received a US Senate Special Committee on Aging 2008 Award and a NIST Bronze Medal Award 2009.